# Evidence for Young Volcanism on Mercury from the Third MESSENGER Flyby

Louise M. Prockter, *et al.*

*Science* **329**, 668 (2010);
DOI: 10.1126/science.1188186

time scale, ~2 min. The tail flux contents at the time of the peak loading events measured by MESSENGER correspond to at least ~30%, and for the most intense event possibly 100%, of the available magnetic flux from Mercury. Such an extreme magnetospheric configuration has never been observed or inferred to be present on the basis of space measurements at Earth or at other planets. The typical fraction of Earth's total magnetic flux that is contained in the tail during loading events that produce intense substorms is only ~10 to 12% (*14*). If Mercury's dayside magnetosphere is fully depleted by reconnection, which may have occurred during event 3, the entire dayside surface would map to open magnetic field lines and be exposed to the shocked solar wind of the magnetosheath.

The close correspondence between the 2- to 3-min duration of the tail-loading and tail-unloading events observed during the third flyby and the ~2-min Dungey cycle time at Mercury suggests not only that Earth-like substorms occur at Mercury but also that plasma circulation times determine the temporal scale for substorms at both planets. Further, the relative variation in tail energy content observed during loading and unloading at Mercury was an order of magnitude larger than at Earth, implying that the relative energy release in substorms at Mercury must be large compared to terrestrial substorms. The high rate of reconnection inferred from the large magnetopause-normal magnetic fields seen during MESSENGER's second flyby (*5*), the large flux transfer events (FTEs) observed just outside Mercury's magnetopause (*25*) by MESSENGER during its earlier flybys (*5*), and the expected low electrical conductivity of Mercury's crust—which should greatly limit line-tying effects (*26*) and allow rapid magnetic flux transfer between the dayside magnetosphere and the tail—are the most likely causes of this intense tail loading. For example, 10 FTEs comparable to the largest flux transfer events measured during the second flyby concentrated over a period of ~1 to 2 min, or 1 FTE every 6 to 12 s, would contribute ~2 MWb to the tail loading, a substantial fraction of the flux addition marking the events during MESSENGER's third flyby. The intense fluxes of higher-energy electrons reported by Mariner 10 (*27*, *28*) and the observations of strong tail loading and unloading and plasmoid ejection reported here, which we attribute to substorm behavior, make the lack of energetic charged particles with energies above 36 keV in the MESSENGER observations for this and earlier flybys (*29*) very surprising. The production of energetic particle acceleration events at Mercury, such as that observed by Mariner 10, evidently requires conditions not yet encountered by MESSENGER.

### References and Notes


1. D. N. Baker, T. I. Pulkkinen, V. Angelopoulos, W. Baumjohann, R. L. McPherron, *J. Geophys. Res.* **101**, 12975 (1996).
2. C. T. Russell, R. L. McPherron, *Space Sci. Rev.* **15**, 205 (1973).
3. V. Angelopoulos *et al.*, *Science* **321**, 931 (2008).
4. G. L. Siscoe, N. F. Ness, C. M. Yeates, *J. Geophys. Res.* **80**, 4359 (1975).
5. J. A. Slavin *et al.*, *Science* **324**, 606 (2009).
6. J.-H. Shue *et al.*, *J. Geophys. Res.* **102**, 9497 (1997).
7. Magnetopause crossings were fit to the model of Shue *et al.* (*6*), with $\alpha = 0.5$ and $R_o = 1.3\ R_M$, where $\alpha$ is the surface flaring parameter and $R_o$ is the distance to the subsolar magnetopause.
8. J. A. Slavin *et al.*, *Geophys. Res. Lett.* **36**, L02101 (2009).
9. Bow-shock crossings were fit to the model of Slavin *et al.* (*8*), with $X_o = 0.475$, $\varepsilon = 1.04$, and $L = 2.59\ R_M$, where $X_o$ is the location of the hyperbola's focus along the aberrated $X_{MSO}$ axis, $\varepsilon$ is the surface's eccentricity, and $L$ is the semi-latus rectum.
10. B. J. Anderson *et al.*, *Space Sci. Rev.* **131**, 417 (2007).
11. S. A. Boardsen *et al.*, *Geophys. Res. Abstr.* **12**, EGU2010-5198-1 (2010).
12. H. Hasegawa *et al.*, *Nature* **430**, 755 (2004).
13. P. M. Trávníček *et al.*, *Icarus* 10.1016/j.icarus.2010.01.008 (2010).
14. S. E. Milan *et al.*, *J. Geophys. Res.* **109**, A04220 (2004).
15. C.-S. Huang, A. D. DeJong, X. Cai, *J. Geophys. Res.* **114**, A07202 (2009).
16. D. Odstrcil *et al.*, *Eos* **90** (fall meet. suppl.), abstract P24A-02 (2009).
17. I. I. Alexeev *et al.*, *Icarus* 10.1016/j.icarus.2010.01.024 (2010).
18. E. W. Hones Jr. *et al.*, *Geophys. Res. Lett.* **11**, 5 (1984).
19. J. A. Slavin *et al.*, *J. Geophys. Res.* **108**, 10.1029/2002JA009557 (2003).
20. A. Kidder, R. M. Winglee, E. M. Harnett, *J. Geophys. Res.* **113**, A09223 (2008).
21. M. B. Moldwin, W. J. Hughes, *J. Geophys. Res.* **98**, 81 (1993).
22. J. A. Slavin *et al.*, *J. Geophys. Res.* **110**, A06207 (2005).
23. B. J. Anderson *et al.*, *Science* **321**, 82 (2008).
24. B. J. Anderson *et al.*, *Space Sci. Rev.* **154**, 307 (2010).
25. J. A. Slavin *et al.*, *Geophys. Res. Lett.* **37**, L02105 (2010).
26. K.-H. Glassmeier, *Planet. Space Sci.* **45**, 119 (1997).
27. D. N. Baker, J. A. Simpson, J. H. Eraker, *J. Geophys. Res.* **91**, 8742 (1986).
28. S. P. Christon, J. Feynman, J. A. Slavin, in *Magnetotail Physics*, A. T. Y. Lui, Ed. (Johns Hopkins Univ. Press, Baltimore, 1987), pp. 393–400.
29. R. D. Starr *et al.*, *Eos* **90** (fall meet. suppl.), abstract P21A-1195 (2009).



30. We thank all those who contributed to the success of the MESSENGER flybys of Mercury. We thank J. Feggans and M. Marosy for data visualization and graphics support. The MESSENGER project is supported by the NASA Discovery Program under contracts NAS5-97271 to the Johns Hopkins University Applied Physics Laboratory and NASW-00002 to the Carnegie Institution of Washington. Small parts of the work were supported by an NSF Center for Integrated Space Weather Modeling grant.

8 February 2010; accepted 25 May 2010
Published online 15 July 2010;
10.1126/science.1188067
Include this information when citing this paper.


# Evidence for Young Volcanism on Mercury from the Third MESSENGER Flyby


**Louise M. Prockter,[1]* Carolyn M. Ernst,[1] Brett W. Denevi,[2] Clark R. Chapman,[3] James W. Head III,[4] Caleb I. Fassett,[4] William J. Merline,[3] Sean C. Solomon,[5] Thomas R. Watters,[6] Robert G. Strom,[7] Gabriele Cremonese,[8] Simone Marchi,[9] Matteo Massironi[10]**



During its first two flybys of Mercury, the MESSENGER spacecraft acquired images confirming that pervasive volcanism occurred early in the planet's history. MESSENGER's third Mercury flyby revealed a 290-kilometer-diameter peak-ring impact basin, among the youngest basins yet seen, having an inner floor filled with spectrally distinct smooth plains. These plains are sparsely cratered, postdate the formation of the basin, apparently formed from material that once flowed across the surface, and are therefore interpreted to be volcanic in origin. An irregular depression surrounded by a halo of bright deposits northeast of the basin marks a candidate explosive volcanic vent larger than any previously identified on Mercury. Volcanism on the planet thus spanned a considerable duration, perhaps extending well into the second half of solar system history.


Images obtained by the MErcury Surface, Space ENvironment, GEochemistry, and Ranging (MESSENGER) spacecraft (*1*) during its first and second flybys of Mercury in 2008 established the presence and diversity of volcanism on Mercury early in the planet's history and indicated an association with ancient impact basins. A key missing element in our understanding of Mercury's global thermal evolution is the temporal extent of volcanic activity and, in particular, the timing of most recent activity (*2*). Previous analyses of the duration of geological activity led to the conclusion (*3*) that volcanism ended before the beginning of Mercury's Mansurian Period, ~3.5 to 1.0 Ga (billion years ago). Here, we report on images obtained during MESSENGER's third Mercury flyby on 29 September 2009 of what may be among the youngest volcanic deposits on the planet.

During that most recent flyby, a ~290-km-diameter peak-ring (double-ring) impact basin, centered at 27.6°N, 57.6°E, was recognized (Fig. 1) (*4*). In terms of size, morphology, and state of preservation, the basin, named Rachmaninoff, closely resembles the 265-km-diameter Raditladi peak-ring basin (27°N, 119°E) that was imaged during MESSENGER's first Mercury flyby (*5*) and may have formed as recently as 1 Ga (*6*). Peak-ring basins are characterized by an outermost basin rim and an interior ring of contiguous peaks and are transitional in form between complex craters and large multiring basins, which contain three or more rings. Peak-ring basins are common on Mercury (*7*), which has the highest density of peak-ring basins among the Moon, Earth, Mars, and Venus (*8*). Rachmaninoff may be transitional between a peak-ring basin and a multiring basin in that it has a partial third ring to the southwest, spanning an arc of about 120°. The inner ring of Rachmaninoff is about 130 km in diameter and slightly elongated in the north-south direction. The basin is surrounded by a continuous ejecta deposit and numerous secondary crater chains. Although it has no visible rays, its ejecta deposit, rim crest, wall terraces, and peaks are crisp and well preserved. On these grounds, the basin is younger than most other basins on Mercury and likely formed well after the end of the late heavy bombardment of the inner solar system at about 3.8 Ga (*3*, *6*, *9*).

The floor of Rachmaninoff basin contains several distinct plains units (Fig. 1). A smooth, relatively bright, high-reflectance plains unit has filled much of the floor within the peak ring (inner smooth plains, pink in Fig. 1B), and three relatively lower-reflectance plains units with broadly similar color characteristics are found within the annulus between the peak ring and the rim (annular smooth plains, green in Fig. 1B; annular hummocky plains, dark blue; and annular low-reflectance plains, purple; collectively hereafter grouped as "annular plains"). The bright, high-reflectance properties of the inner smooth plains are nearly identical to those of a large expanse of smooth plains located to the northeast of the basin that embay and are thus younger than Rachmaninoff ejecta. Although smooth plains with similar color properties are common within craters and basins elsewhere on Mercury (*10*), only one other example has been found to date where these types of plains appear confined within a basin's central peak ring (the 225-km-diameter Renoir basin).

There is no apparent difference in color and reflectance between the annular plains units and the basin peak ring and terrace material (peak-ring material, light gray, and terrace material, light blue; Fig. 1B), all of which are up to 28% lower in reflectance than the inner smooth plains (Fig. 1C). These characteristics are consistent with those of low-reflectance material observed elsewhere on Mercury both as scattered deposits and concentrated in the central peaks and ejecta deposits of craters and basins such as Tolstoj (*10*, *11*) (16°S, 195°E).

The geological characteristics of these units (Fig. 1B) provide further information on their origin. The plains units in the annulus between the peak ring and the basin wall are similar to typical rough-textured, hummocky units that characterize the floors of complex craters and basins on the Moon and Mercury (*7*, *12*, *13*). During the

[1]Johns Hopkins University Applied Physics Laboratory, Laurel, MD 20723, USA. [2]School of Earth and Space Exploration, Arizona State University, Tempe, AZ 85251, USA. [3]Southwest Research Institute, 1050 Walnut Street, Boulder, CO 80302, USA. [4]Department of Geological Sciences, Brown University, Providence, RI 02912, USA. [5]Department of Terrestrial Magnetism, Carnegie Institution of Washington, Washington, DC 20015, USA. [6]Center for Earth and Planetary Studies, National Air and Space Museum, Smithsonian Institution, Washington, DC 20013, USA. [7]Lunar and Planetary Laboratory, University of Arizona, Tucson, AZ 85721, USA. [8]Instituto Nazionale di Astrofisica–Astronomical Observatory of Padova, 35122 Padova, Italy. [9]Department of Astronomy, University of Padova, 35137 Padova, Italy. [10]Department of Geoscience, University of Padova, 35137 Padova, Italy.

*To whom correspondence should be addressed. E-mail: Louise.Prockter@jhuapl.edu

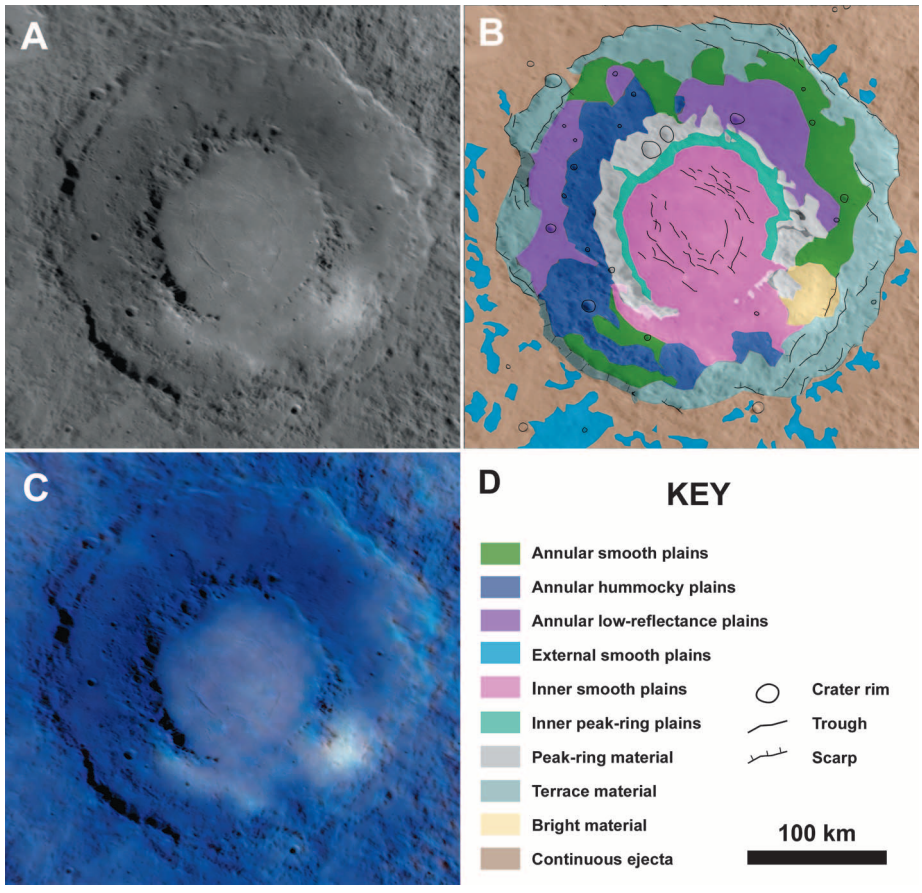


**Fig. 1.** Rachmaninoff peak-ring basin. (**A**) MDIS narrow-angle camera (NAC) mosaic (images 0162744128 and 0162744150); orthographic projection centered at 27.6°N, 57.6°E. (**B**) Geological sketch map of Rachmaninoff overlaid on (A), showing the variety of plains units in and around the basin. North is up. (**C**) Enhanced-color view (second and first principal components and 430-nm/1000-nm ratio in red, green, and blue, respectively) of Rachmaninoff basin imaged with the MDIS wide-angle camera (WAC) during MESSENGER's third flyby of Mercury (WAC images 162741039 to 162741083). Lower-resolution WAC observations (5 km per pixel) were merged with the higher-resolution NAC mosaic (~440 m per pixel) to display color variations with geologic terrain. (**D**) Map legend.

early modification stage of the cratering event that forms such structures, impact melt lines the interior of the crater cavity, drapes over the ejecta blocks, drains into lows, ponds to form smooth plains, and solidifies. In lunar basins, the color of the melt unit is commonly similar to that of the ejecta (*13*). Similar characteristics are seen in Rachmaninoff peak-ring basin (Fig. 1B), where annular hummocky deposits (dark blue unit; Fig. 1B) are concentrated outside of the uplifted peaks of the peak ring, and annular smooth and low-reflectance plains (green and purple units; Fig. 1B) are concentrated in the low topography along the base of the terraced wall. On the basis of these observations, we interpret Rachmaninoff annular plains to be derived from impact melt.

In many fresh peak-ring and multiring basins on the Moon and Mercury, the plains interior to the peak ring are similar in reflectance, morphology, and color properties to smooth plains in the annulus and are thus also thought to be solidified impact melt (*7*, *12*–*14*). An impact-melt origin has been proposed for the plains found within Raditladi, which appear to be similar in age to the basin (*5*).

The inner smooth plains of Rachmaninoff basin, however, differ from surrounding units in their reflectance, color properties, embayment relations, structural characteristics, and density of superposed craters. The inner smooth plains have embayed the foot of the peak ring and have obscured its southern part (Fig. 1). On the basis of these associations, we interpret the plains to have formed from fluid material that flowed across the peak ring to partly flood the units in the surrounding annulus in the southern part of the crater. These characteristics imply that the smooth plains within the peak ring formed from volcanic activity subsequent to the formation of Rachmaninoff basin. A narrow (10 to 20 km wide) region of low-reflectance smooth material (inner peak-ring plains, turquoise unit; Fig. 1B) just inside the peak ring at the outer edge of the inner smooth plains is reminiscent of geometrical arrangements in lunar impact basins that have subsided as a combined result of subsurface cooling (*15*), volcanic flooding, and embayment of the topographic low (*13*, *16*), and lithospheric flexure in response to the volcanic load (*16*). This unit could also have resulted from mass wasting of the peak ring onto the inner smooth plains.

Further evidence for volcanism in this region comes from the presence of a bright, high-reflectance patch located along the southeastern margin of the plains in the annulus between Rachmaninoff's peak ring and outer rim (bright material, yellow; Fig. 1B). The bright patch appears to be associated with rough-textured, hummocky material, which may be part of the deposit or may reflect underlying terrain over which the material is draped. The bright material is char-

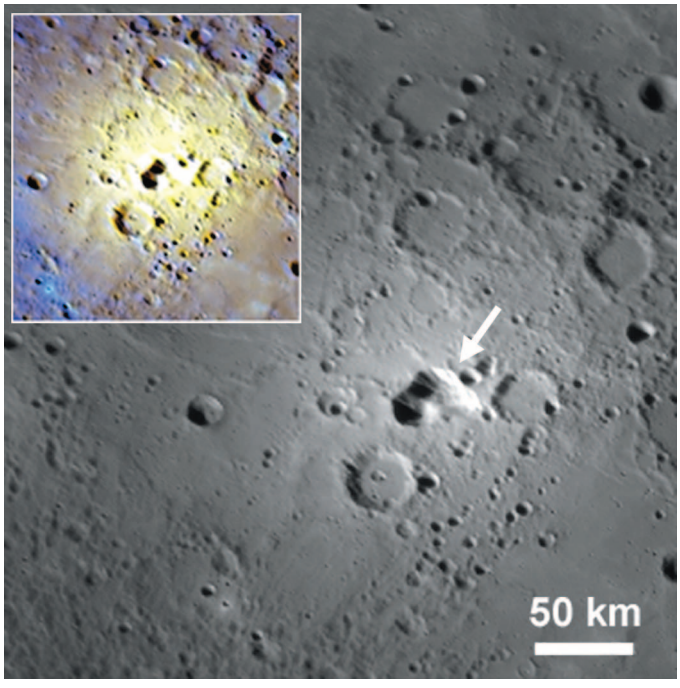


**Fig. 2.** MDIS NAC image of a diffuse, high-reflectance halo over 200 km in extent surrounding a ~30-km-diameter, irregularly shaped, rimless, steep-walled depression (arrow) (image 162744128). (**Inset**) Enhanced-color view (as in Fig. 1C) showing the bright halo overlying a high-reflectance smooth plains unit that embays Rachmaninoff to the north and east. Equirectangular projection centered at 27°N, 57°E (WAC images 162741039 to 162741083); north is up.

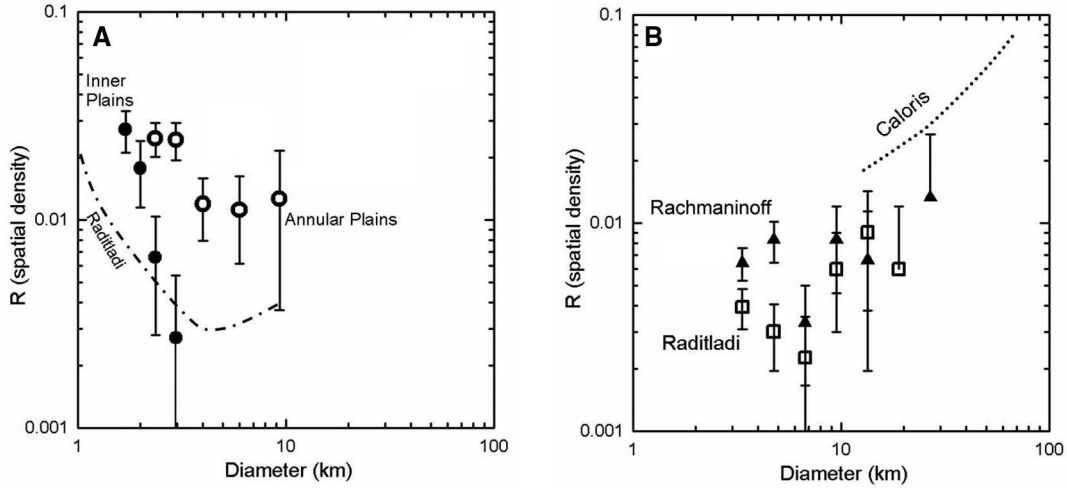


**Fig. 3.** Size-frequency distributions of impact craters superimposed on the Rachmaninoff and Raditladi peak-ring basins and on the plains inside Rachmaninoff [supporting online material (SOM)]. Error bars are proportional to $\sqrt{N}/N$, where $N$ is the number of craters per given area within an increment in diameter $D$. (**A**) R plot of the spatial density of craters within the inner peak ring of Rachmaninoff (solid symbols, excluding probable endogenic crater-form depressions associated with the graben) compared with that for the annular plains between the peak ring and the main basin rim of Rachmaninoff (open symbols) (*25*). Shown for comparison is a curve approximately fitting the size distribution for craters on the younger smooth plains within Raditladi basin (dash-dot curve) [figure 3 of (*6*)]. The data for Raditladi are described in more detail in the SOM. (**B**) R plot of the spatial density of craters on Rachmaninoff basin and its immediate ejecta (triangles), excluding the inner plains unit; these data are interpreted to represent the stratigraphic age of the Rachmaninoff impact. Similar measurements on Raditladi basin and its immediate ejecta (open squares) reveal that Rachmaninoff is resolvably older than Raditladi. The dotted line shows the approximate size-frequency distribution for the rim of Caloris basin (*26*).

acterized by a diffuse distribution, a steep slope of the reflectance spectrum from visible to near-infrared wavelengths, and a reflectance 20% higher than that of high-reflectance plains to the north of the basin. About 480 km to the northeast of Rachmaninoff, a similar high-reflectance, diffuse halo over 200 km in extent surrounds an ~30-km-diameter, irregularly shaped, rimless, steep-walled depression (Fig. 2). The material within this halo deposit is nearly 70% higher in reflectance than the high-reflectance plains to the north, placing it among the highest-reflectance features observed on the planet, including the fresh ejecta of Kuiperian craters (*17*). Although the distinctive color of the deposit could be interpreted as the result of more space weathering than has affected fresh crater ejecta, the combination of an especially steep spectral slope and very high reflectance implies that the deposit has a different composition or physical properties and that its color is not due to space weathering.

The reflectance properties of these halo deposits are similar to those of spectrally distinct deposits observed elsewhere on Mercury in association with crater and basin interiors and interpreted to be products of pyroclastic volcanism (*18*). Scalloped depressions similar to the one northeast of Rachmaninoff basin have been identified elsewhere on Mercury, notably just inside the rim of Caloris basin (e.g., at 22.4°N, 146.3°E), and have been interpreted as sites of explosive volcanic activity (*18*–*21*) where bright material was emplaced ballistically around a central source vent. The scalloped depression northeast of Rachmaninoff is remarkable in that it is not only larger than the largest previously identified candidate vent around the rim of Caloris, but its surrounding halo of bright material extends twice as far as the deposit around that vent (*18*). We do not find any scalloped depression that could be interpreted as a candidate source vent for the bright patch within the Rachmaninoff annulus, however.

Deformation postdated volcanism within Rachmaninoff basin. Lying within the inner smooth plains unit is a set of narrow extensional troughs or graben (Fig. 1B). Extensional faulting on Mercury is rare and generally confined to impact basins (*22*, *23*). The pattern of graben in Rachmaninoff is similar to that in Raditladi, where the graben are dominantly basin-concentric and form an incomplete ring that is offset from the center of the basin (*5*). The cumulative length of imaged graben in Rachmaninoff (~460 km) is larger than in Raditladi (~180 km), indicating that the floor of Rachmaninoff experienced greater extensional strain. The extension within Rachmaninoff and Raditladi basins likely accompanied uplift of the basin floors, as is thought to be the case for the larger Caloris and Rembrandt basins (*22*, *23*). The observation that the extensional troughs in Rachmaninoff are confined to the volcanic inner plains suggests that the volcanism and uplift may have been related.

The very small number of superposed craters indicates that the inner smooth plains within Rachmaninoff basin may be among the youngest volcanic deposits on Mercury. The volcanism must postdate the cratering event because the inner plains embay or overlie units related to basin formation. To assess the time interval between basin formation and volcanism, we measured the size-frequency distribution of impact craters superposed on the inner and annular plains. The inner plains of Rachmaninoff are less cratered than the annular plains and hence younger, a difference that is particularly noticeable for craters greater than ~2 to 3 km in diameter (which are unambiguously resolvable and difficult to remove by later geological activity). This result is consistent with a volcanic origin for the inner plains. The differences in the trends of the size-frequency distributions at crater diameters of 2 to 3 km between the two areas may reflect that craters of these sizes are most likely secondary craters with uneven population statistics (*6*). Comparison of crater counts in areas associated with formation of Rachmaninoff basin (the annular plains, rim deposits, and inner ejecta blanket) with similar measurements for Raditladi basin (Fig. 3B) suggest that Rachmaninoff basin formed somewhat earlier than Raditladi basin. Although the crater size-frequency distributions for Raditladi and the two units within Rachmaninoff do not follow precisely the same trends, the inner plains of Rachmaninoff are older than the floor of Raditladi but substantially younger than the Rachmaninoff annular plains.

In principle, we may estimate absolute ages for Rachmaninoff basin and its related units by comparing these size-frequency distributions with models for the rate of production of craters on Mercury (*9*, *24*). Such models depend on differences in flux and impactor energies between the Moon and Mercury, and assumptions about the properties of the surfaces impacted, and adopted scaling relationships, and they are influenced by uncertainties in the size distribution of inner solar system asteroids. Whereas interpretations after Mariner 10 were that plains formation on Mercury ceased shortly after the end of the late heavy bombardment (~3.8 Ga), volcanism within Rachmaninoff (and formation of the plains within the younger Raditladi basin) extended well into the Mansurian and conceivably to times as recent as ~1 Ga. Models for crater retention age (*9*, *24*) involve primary cratering only, and most of the craters on the smooth plains in Fig. 3A may be secondary craters, given the pronounced steep slope of their size-frequency distribution (*6*). For this reason, the volcanism and associated deformation within Rachmaninoff could have ended even more recently.

### References and Notes


1. S. C. Solomon, R. L. McNutt Jr., R. E. Gold, D. L. Domingue, *Space Sci. Rev.* **131**, 3 (2007).
2. J. W. Head *et al.*, *Space Sci. Rev.* **131**, 41 (2007).
3. P. D. Spudis, J. E. Guest, in *Mercury*, F. Vilas, C. R. Chapman, M. S. Matthews, Eds. (Univ. of Arizona Press, Tucson, 1988), pp. 118–164.
4. Rachmaninoff and its surroundings were imaged at ~440 m per pixel with MESSENGER's Mercury Dual Imaging System (MDIS) monochrome narrow-angle camera and at 5 km per pixel with the 11 filters of the MDIS wide-angle camera, which span wavelengths from 400 to 1040 nm (*27*).
5. L. M. Prockter *et al.*, *Lunar Planet. Sci.* **40**, abstr. 1758 (2009).
6. R. G. Strom, C. R. Chapman, W. J. Merline, S. C. Solomon, J. W. Head III, *Science* **321**, 79 (2008).
7. R. J. Pike, in *Mercury*, F. Vilas, C. R. Chapman, M. S. Matthews, Eds. (Univ. of Arizona Press, Tucson, 1988), pp. 165–273.
8. C. A. Wood, J. W. Head, *Proc. Lunar Sci. Conf.* **7**, 3629 (1976).
9. M. Massironi *et al.*, *Geophys. Res. Lett.* **36**, L21204 (2009).
10. B. W. Denevi *et al.*, *Science* **324**, 613 (2009).
11. M. S. Robinson *et al.*, *Science* **321**, 66 (2008).
12. M. J. Cintala, R. A. F. Grieve, *Meteorit. Planet. Sci.* **33**, 889 (1998).
13. J. W. Head *et al.*, *J. Geophys. Res.* **98**, 17149 (1993).
14. P. D. Spudis, *The Geology of Multi-Ring Basins* (Cambridge Univ. Press, New York, 1993).
15. S. R. Bratt, S. C. Solomon, J. W. Head, *J. Geophys. Res.* **90**, 12415 (1985).
16. S. C. Solomon, J. W. Head, *Rev. Geophys. Space Phys.* **18**, 107 (1980).
17. C. R. Chapman, in *Mercury*, F. Vilas, C. R. Chapman, M. S. Matthews, Eds. (Univ. of Arizona Press, Tucson, 1988), pp. 1–23.
18. L. Kerber *et al.*, *Earth Planet. Sci. Lett.* **285**, 263 (2009).
19. J. W. Head *et al.*, *Science* **321**, 69 (2008).
20. S. L. Murchie *et al.*, *Science* **321**, 73 (2008).
21. J. W. Head *et al.*, *Earth Planet. Sci. Lett.* **285**, 227 (2009).
22. T. R. Watters *et al.*, *Earth Planet. Sci. Lett.* **285**, 309 (2009).
23. T. R. Watters *et al.*, *Science* **324**, 618 (2009).
24. S. Marchi, S. Mottola, G. Cremonese, M. Massironi, E. Martellato, *Astron. J.* **137**, 4936 (2009).
25. In an R plot, the differential crater size-frequency distribution $N(D)$ is divided by the power law $dN(D) \sim D^{-3}dD$, where $N$ is the number of craters within an increment of crater diameter $D$ per given area.
26. C. I. Fassett *et al.*, *Earth Planet. Sci. Lett.* **285**, 297 (2009).
27. S. E. Hawkins III *et al.*, *Space Sci. Rev.* **131**, 247 (2007).


28. We are grateful to N. Chabot, N. Laslo, and H. Kang, who designed the imaging sequences that made this contribution possible, and to the tireless efforts of the engineers and technical support personnel on the MESSENGER team. The MESSENGER project is supported by the NASA Discovery Program under contracts NASW-00002 to the Carnegie Institution of Washington and NAS5-97271 to the Johns Hopkins University Applied Physics Laboratory.


### Supporting Online Material

www.sciencemag.org/cgi/content/full/science.1188186/DC1
SOM Text
Fig. S1
Table S1


10 February 2010; accepted 7 July 2010
Published online 15 July 2010;
10.1126/science.1188186
Include this information when citing this paper.